applied sciences

MDPI

Article

A Reaction Microscope for AMO Science at Shanghai Soft X-ray Free-Electron Laser Facility

Wenbin Jiang [1,2], Xincheng Wang [3,*], Shuai Zhang [2,4], Ruichao Dong [1,2], Yuliang Guo [1,3], Jinze Feng [3], Zhenjie Shen [1], Zhiyuan Zhu [2,4] and Yuhai Jiang [1,2,3,*]

1 Shanghai Advanced Research Institute, Chinese Academy of Sciences, Shanghai 201210, China; jiangwenbin@sari.ac.cn (W.J.); dongrc@sari.ac.cn (R.D.); guoyl@sari.ac.cn (Y.G.); shenzhj@sari.ac.cn (Z.S.)
2 University of Chinese Academy of Sciences, Beijing 100049, China; zhangshuai2@shanghaitech.edu.cn (S.Z.); zhuzhiyuan@sinap.ac.cn (Z.Z.)
3 Center for Transformative Science, School of Physical Science and Technology, ShanghaiTech University, Shanghai 201210, China; fengjz@shanghaitech.edu.cn
4 Shanghai Institute of Applied Physics, Chinese Academy of Sciences, Shanghai 201800, China
* Correspondence: wangxch1@shanghaitech.edu.cn (X.W.); jiangyh3@shanghaitech.edu.cn (Y.J.)

Abstract: We report on the design and capabilities of a reaction microscope (REMI) end-station at the Shanghai Soft X-ray Free-Electron Laser Facility (SXFEL). This apparatus allows high-resolution and 4π solid-angle coincidence detection of ions and electrons. The components of REMI, including a supersonic gas injection system, spectrometer, detectors and data acquisition system, are described in detail. By measuring the time of flight and the impact positions of ions and electrons on the corresponding detectors, three-dimensional momentum vectors can be reconstructed to study specific reaction processes. Momentum resolutions of ions and electrons with 0.11 a.u. are achieved, which have been measured from a single ionization experiment of oxygen molecules in an infrared (IR), femtosecond laser field, under vacuum at 1.2×10^{-10} torr, in a reaction chamber. As a demonstration, a Coulomb explosion experiment of oxygen molecules in the IR field is presented. These results demonstrate the performance of this setup, which provides a basic tool for the study of atomic and molecular reactions at SXFEL.

Keywords: reaction microscope; free-electron laser; Coulomb explosion

Citation: Jiang, W.; Wang, X.; Zhang, S.; Dong, R.; Guo, Y.; Feng, J.; Shen, Z.; Zhu, Z.; Jiang, Y. A Reaction Microscope for AMO Science at Shanghai Soft X-ray Free-Electron Laser Facility. *Appl. Sci.* **2022**, *12*, 1821. https://doi.org/10.3390/app12041821

Academic Editor: Kiyoshi Ueda

Received: 20 January 2022
Accepted: 3 February 2022
Published: 10 February 2022

1. Introduction

A reaction microscope (REMI), or cold-target recoil-ion momentum spectroscopy (COLTRIMS), is/uses a device designed to measure the momenta of charged reaction fragments in coincidence [1–4]. In 1987, the first system of spectrometers to detect recoil ions using static gas as a target, at room temperature, was built by J. Ullrich et al. [5]. A uniform magnetic field generated by a pair of Helmholtz coils, having been introduced a few years later, measures electrons with a 4π solid angle [6,7]. Since then, kinematically complete experiments have become possible and the continuous development of supersonic gas jet technology [8–10] and detector technology, based on a micro-channel plate and delay-line anode, has greatly improved momentum resolution [11–14]. After development of more than three decades, this technology has become mature and is presently widespread. By measuring the energies and emission angles of charged products with high precision, detailed information can be obtained for deeper investigation of atomic and molecular reactions with ions, electrons or photons.

In the past 10 years, REMI/COLTRIMS has been employed for a tremendous amount of studies in synchrotron radiation. On the other hand, with the rapid innovation of laser technology, especially chirped pulse amplification technology [15], ultra-short laser pulses at high intensities have provided extraordinary experimental conditions for the study of atomic, molecular and optical (AMO) physics. Through the combination of reaction

microscopes and laser devices [16–18], many physical phenomena of the reactions of gas targets with photons have been explored, such as multi-photon ionization, above-threshold ionization, tunneling ionization, high harmonic generation (HHG) and so on. As a new generation of coherent light source, X-ray free-electron lasers (FEL) have the characteristics of high power, a wide and continuously tunable wavelength, short pulses and good coherence, serving a number of applications in various areas of science [19,20]. In AMO science, the most far-reaching applications are manifested in the topics of nonlinearity induced by single- or many-photon absorption, and the ultrafast molecular dynamics and structural imaging of a single molecule in the regime of UV-to-hard-X-ray photons [21–25]. Few-photon induced atomic and molecular dynamics [26–30] and isomerization [31,32] have been studied in detail. Some exotic physical phenomena, such as the "hollow atoms" [33] and the "molecular black hole" [34] have been observed recently. The former is formed by quickly ejecting a few inner-shell electrons, resulting in the phenomenon of "transparency" to X-rays [35]. In the latter case, the X-ray pulse first strips the number of electrons from a heavy atom, due to its huge cross section, and then a highly positive resulting charge traps electrons from neighboring atoms within the molecule. X-ray lasers can also ionize a number of electrons from one heavy atom within a large biomolecule, which leads to the rapid redistribution of electrical charge in a tiny time window and provides rich information for analyzing biomolecules using X-ray lasers. Further, some basic physical processes of atoms and molecules have been reached using X-ray lasers with the control of wavelength, phase and intensity [36,37]. Moreover, the circularly polarized light generated in free-electron lasers is used to study the circular dichroism of atoms, linear molecules and chiral molecules [38–40]. More recently, experimental studies were extended to the photoelectron diffraction imaging in a molecular breakup frame using an X-ray FEL [41].

The construction of the Shanghai Soft X-ray Free-Electron Laser Facility (SXFEL) began in 2014. Two beamlines, including the seeded line and SASE line, together with five end stations, including cell imaging, AMO, ultrafast physics and surface chemistry, are expected to be put into user operation in 2022 [42]. Its focused free-electron laser beam with high pulse intensity ($>10^{14}$ W/cm^3) and high single-photon energy (100–600 eV) brings a new opportunity for the research of AMO physics. The reaction microscope introduced, here, is installed at the south branch of the seeded FEL line currently and all the endstations are movable in principle, thus, experiments at the SASE beamline are also possible. Multi-particle coincidence detection can be realized by REMI for both ions and electrons, featuring a high collection rate, wide energy detection range and high resolution. These advantages make the instrument ideal for coincident experiments on atoms and molecules. Limited by the low repetition of SXFEL, at present, REMI may be proper for measurements of molecules with heavy atoms. Here we introduce is principles, design, structure and test results, using an infrared femtosecond laser.

2. Apparatus Setup

2.1. Overview

The setup we present here is mainly composed of a vacuum system, a supersonic gas jet system, a spectrometer system and the data acquisition system. Atoms or molecules are collimated and cooled to form a supersonic target and react with the focused laser. Then, the ions and electrons are accelerated and guided onto opposing detectors by electric and magnetic fields. The three-dimensional momentum vector of each particle is accurately reconstructed from the particle's arrival position (X,Y) and TOF at the detector.

To get a good resolution, a cold supersonic gas beam is essential to decrease the thermal momentum spread. The gas from the high-pressure gas bottle is forced into the low pressure vacuum chamber. Through two skimmers and two pairs of slits perpendicular to each other, a thin gas target is formed in the intersection chamber (science chamber). A multistage vacuum system is used to maintain a typical vacuum of 1.2×10^{-10} torr in the science chamber. The schematic picture is shown in Figure 1. A uniform electric field from the spectrometer, along with the uniform magnetic field generated by a pair of Helmholtz

coils (orange) are applied to guide the recoil ions and electrons to the bilateral detectors. The details of key components of this apparatus are introduced in the following section.

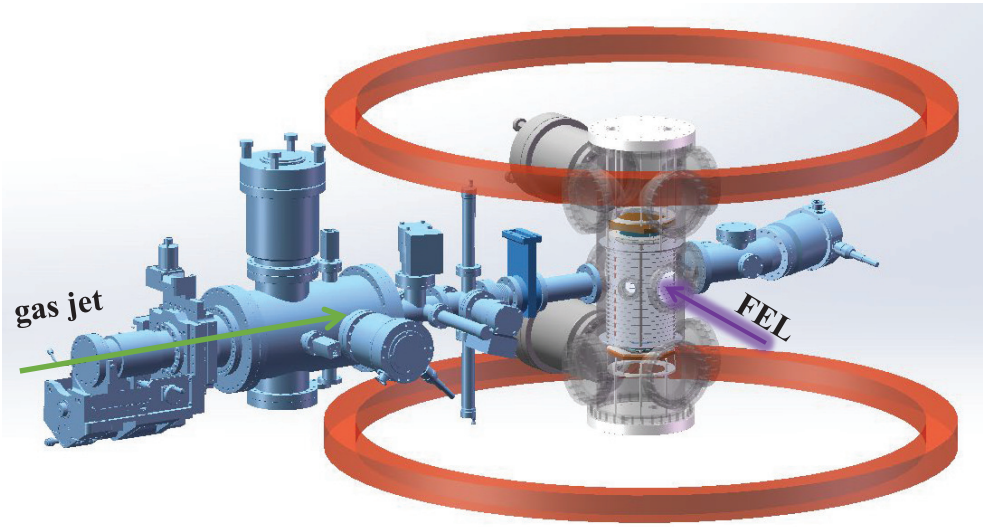

Figure 1. Overview of the REMI at SXFEL. A mutually perpendicular gas jet line (green arrow) and FEL line (purple arrow) meet in the intersection chamber, which contains the spectrometer and detectors. A pair of coils (orange) is used to constrain the electron trajectory.

2.2. Supersonic Gas Jet

At room temperature, the thermal motion of atoms and molecules in a gas target would bring a great error to the measurement of momentum. Therefore, the formation of a well-localized and internally cold gas target is one of the key factors to ensure high-resolution measurement. In addition, it is desirable to ionize less than one molecule per laser pulse in experiments, in order to make accurate ion–electron coincidence measurements, so, a thin target is required, considering the high power of SXFEL.

The composition of the supersonic gas jet system is depicted in Figure 2. A 50 μm nozzle is installed on a three-dimensional adjustable manipulator. The high-pressure (1–5 bar) gas froma conventional gas cylinder passes into the low-pressure vacuum chamber through the nozzle. The gas in the low-pressure region expands quasistatically and adiabatically so that the enthalpy of the gas is converted into directional kinetic energy. A conical skimmer of 0.2 mm inner diameter is placed at 15-mm downstream of the nozzle to extract the centerline gas beam from the so-called zone of silence. The length of zone of silence during the experiments is estimated to be 30 mm by equation [43]

$$L = \frac{2}{3}\sqrt{\frac{p_0}{p_b}}d_{nozzle}, \tag{1}$$

where p_0 is the initial gas pressure and p_b is the background pressure in the first stage. Subsequently, a skimmer of 0.4 mm in diameter and mounted parallel to the first skimmer selects particles with a small momentum spread in the x and z planes. After that, two pairs of adjustable slits are arranged to tune the size of the gas beam in the direction perpendicular to the jet's propagation direction. An internally cold supersonic gas target is then obtained and the remaining gas is collected in the dumping chamber, which is an independent residual gas extraction system (not shown here). The distance between the nozzle and reaction center is about 1045 mm.

As is shown in Table 1, the whole supersonic gas jet system has six vacuum stages. The low vacuum pressurein the source chamber is gradually transitioned to ultra-high vacuum conditions when reaching the intersection chamber via several differential pumping stages. At the intersection region, the maximum diameter of the gas jet(uncollimated) in the x and z directions is around 4.0 mm, and the size adjustment accuracy is 0.02 mm,

which is determined by the adjustment accuracy of the slits. The density of gas target is estimated to be about $10^8/cm^3$. From the speed ratio, S, of 38.7 in the experiment of the single ionization of He, which is the mean jet velocity divided by the thermal spread in velocities, it is estimated that the gas jet is eventually cooled to 0.5 K [44]. Ultra-high vacuum conditions and a thin gas-jet target make the coincidence measurement of ions and electrons in the strong field of free electron laser feasible.

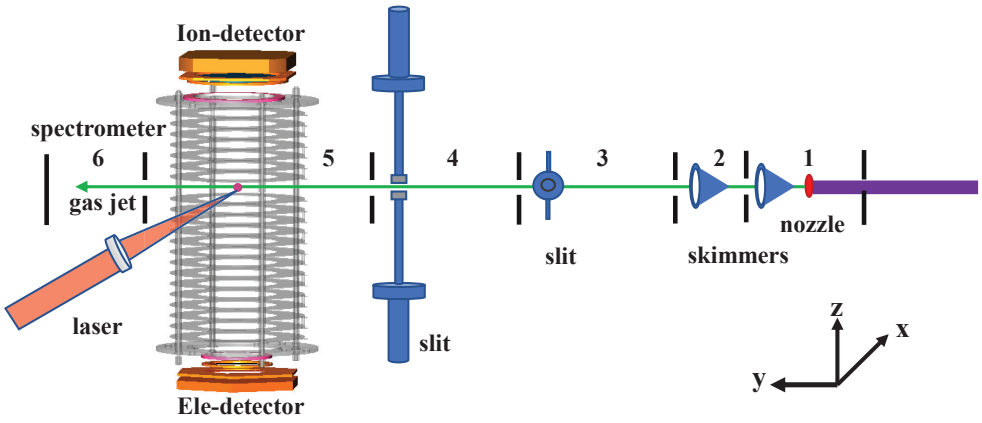

Figure 2. Schematic diagram of supersonic gas-jet system structure. The green arrow represents the propagation direction of the gas jet passing through six chambers from the nozzle to the dumping chamber. After passing through two skimmers and two pairs of slits, the jet collides with the laser (pink) in the center zone of the interaction chamber (purple dot) and is collected in the dumping chamber.

Table 1. Typical pressures of different chambers before and after gas injection. Numbers one through six represent the source, first differential, second differential, third differential, intersection and dumping chambers, respectively. The pressures are given in torr.

Chamber	1	2	3	4	5	6
before injection	1.5×10^{-9}	4.4×10^{-9}	1.3×10^{-9}	9.2×10^{-10}	1.2×10^{-10}	7.2×10^{-11}
after injection	2.7×10^{-3}	1.3×10^{-8}	6.2×10^{-9}	1.0×10^{-9}	1.2×10^{-10}	9.8×10^{-11}

2.3. Spectrometer

Both the reaction between the supersonic gas jet and the laser and the collection of the reaction particles occur in the intersection chamber. The spectrometer, providing a uniform electric field to accelerate ions and electrons, is schematically shown in Figure 3. It consists of 23 pieces of 1-mm-thick stainless steel-ring electrodes of 120 mm inner diameter and 200 mm outer diameter. The rings are separated by an 11-mm distance between each other by insulating ceramics and electrically connected by a cascade of 30-kΩ resistors. Thus, the voltages on each ring electrode are uniformly distributed simply by applying two voltages to the ends of the spectrometer. The length of ion-flight region is 100 mm, while that of electron is 184 mm. The shorter length of ion-acceleration region makes the ion detector more suitable for particles with higher energies, such as recoil ions from the Coulomb explosion of molecules. Two meshes are mounted at both ends of spectrometer to eliminate the influence of the high voltage from the MCPs and to ensure the uniformity of the electric field. The stainless steel grids (wire diameter: 25 μm; mesh size: 292 μm) provide a transmittance of 85%.

For the same momentum, the electron and ion velocities differ by a large mass ratio. Thus, for increasing electron energies, the detection efficiency decreases. Increasing the electric field would reduce the electron-momentum resolution. In order to achieve a 4π solid-angle measurement for high-energetic electrons, a pair of Helmholtz coils is necessary to generate a uniform magnetic field along the spectrometer axis, constraining

the trajectories of the electrons. In this way, electrons will fly in spiral tracks before reaching the detector. Helmholtz coils are a pair of parallel coils with the same radius, number of turns and resistance. The distance between the two coils and the radius of the coils are both 87.5 cm. According to the test, the coils can stably generate a maximum magnetic field of 17 Gs with no air cooling or water cooling.

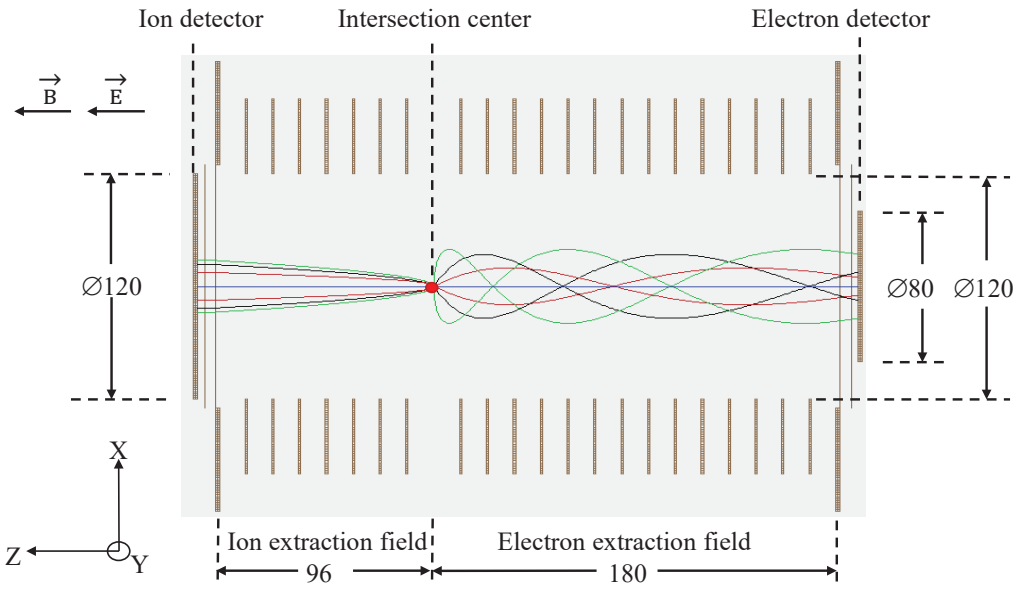

Figure 3. Schematics of REMI including the geometric dimensions (unit: mm) of the REMI. Trajectories of ions and electrons with different emission angles are shown as colored lines.

The effect of the electric and magnetic fields on particle trajectories can be seen in Figure 3. For electrons with an energy of 15 eV and oxygen ions with an energy of 0.2 eV, charged particles towards different directions are all collected by the detector with an electric field of 4 V/cm and a magnetic field of 6 Gs. Then, the three-dimensional momenta of ions and electrons can be reconstructed from the TOF, achieving the detection position of each event.

2.4. Data Acquisition System

To detect the fragment ions and electrons in coincidence, a fast data acquisition system is required. Two MCP detectors equipped with delay-line anodes are employed to measure the arrival time and impact position of the charged fragments [45]. For ion detection, to have a high collection efficiency for Coulomb explosion studies, a pair of larger MCPs (120 mm diameter) is employed with a square delay-line anode (DLD 120, Roentdek). For electron detection, as a result of the small time-of-flight differences, a hexagonal anode is of significant importance in reducing the dead time and increasing detection efficiency [14]. The effective detection area is limited by the diameters of the MCPs and anode about 80 mm (Hex75, Roentdek). It should be noted that a mesh with the same parameter described before is placed in front of each detector to generate a post-acceleration voltage so as to increase the MCP detection efficiency.

The delay-line readout relies on a fast and precise timing measurement. The data-acquisition system combines the data collected from each detector into complete events, which are stored for offline analysis. The positive signals from the MCPs are inverted and then amplified by fast-timing amplifiers (ORTEC FTA820) along with signals from the delay-line anodes. The amplified signals (gain 200) are inputs to the constant-fraction discriminator (ORTEC QUAD935) with a minimum pulse–pair dead-time of 15 ns to discriminate the signal and convert it into a signal in NIM format, which can minimize the influence of changes in the size and shape of the analog signal on signal processing.

A time-to-digital conversion module (Roentdek TDC8HPi) containing two cards is used to convert the input NIM signal into a digital signal. Each card contains eight, high-precision acquisition channels and each channel can perform multi-hit response with a high time resolution of 35 ps RMS with 25 ps LSB (Least Significant Bit). Taking the trigger signal as the time-zero point, all time signals belonging to the same event are stored in the data packet as a whole. The data stored in event-by-event mode can reconstruct complete information of the particle momentum in the offline analysis. The analysis code is embedded in the Go4 (GSI Object Oriented On-line Off-line system) analysis environment (GSI, 2018) based on CERN's ROOT (CERN, 2018). Besides, in the testing phase, we also use the software package CoboldPC (Computer Based Online-offline List-mode Data analyzer for PC) supported by RoentDek to realize the data acquisition and data analysis. The timing resolution achieved is about 1 ns and the position resolution of these detectors is typically about 0.1 mm, which can be improved a bit via careful calibration.

3. Result and Discussion

The test experiments have been performed with an infrared femtosecond laser, which had a wavelength of 800 nm, a pulse width of 35 fs, a focal length of 25 cm and a repetition rate of 1 kHz. Through the single ionization experiment of O_2, the momentum resolution of the ion and electron detectors and the detection range of electron momenta are given. The result of the Coulomb explosion experiment of O_2 demonstrates the performance for multi-particle coincidence detection and the large ion-momentum detection range. Through data analysis, several oxygen Coulomb explosion channels are clearly found and detailed information on their explosion pattern is obtained.

3.1. Single Ionization Experiment of Oxygen Molecules

The 2.3×10^{14} W/cm^2-intensity laser interacted with the oxygen molecules, and photoelectrons and O_2^+ ions were generated in the ionization process. During the experiment, the extraction electric field was set to 1.5 V/cm and the coil current was set to 4.0 A, which produced a magnetic field around 7 Gauss.

Figure 4a shows that most of the ions are O_2^+ from the gas jet. It can be seen in Figure 4b that electrons and O_2^+ ions had a clear correlation in TOF, which represents the momentum conservation between those two particles in the z direction. After selecting the events within the coincidence line and calculating the corresponding momenta, a one-dimensional spectrum was generated by summing the electron momentum and the ion momentum in Figure 4c, and a Gaussian-like distribution was obtained. By fitting the spectrum, as is shown with the red curve, a good agreement with the experimental data was achieved. The full-width-at-half-maximum (FWHM) of the momentum sum spectrum was 0.11 a.u., and this represents the convoluted momentum resolution of the two detectors. Thus 0.11 a.u. was the upper limit of momentum resolution for both electrons and ions in this test. With the position resolution of 0.1 mm, the resolution in the x and y directions could be thus estimated to be 0.13 a.u.

An electron–TOF-radius correlation is presented in Figure 4d, where the radius is the distance between electron impact position and the origin position on the detection plane. The period of the electron cyclotron motion was 49 ns and the corresponding magnetic field was 7.2 Gs. Taking into account the detection area of the electron detector with a diameter of 80 mm, the electron-momentum detection range could be calculated to be within 1.13 a.u. In subsequent tests, it was measured that the device could provide a stable magnetic field of 17 Gs, which corresponds to a momentum detection range of 2.81 a.u. and an energy detection range of 108 eV for electrons.

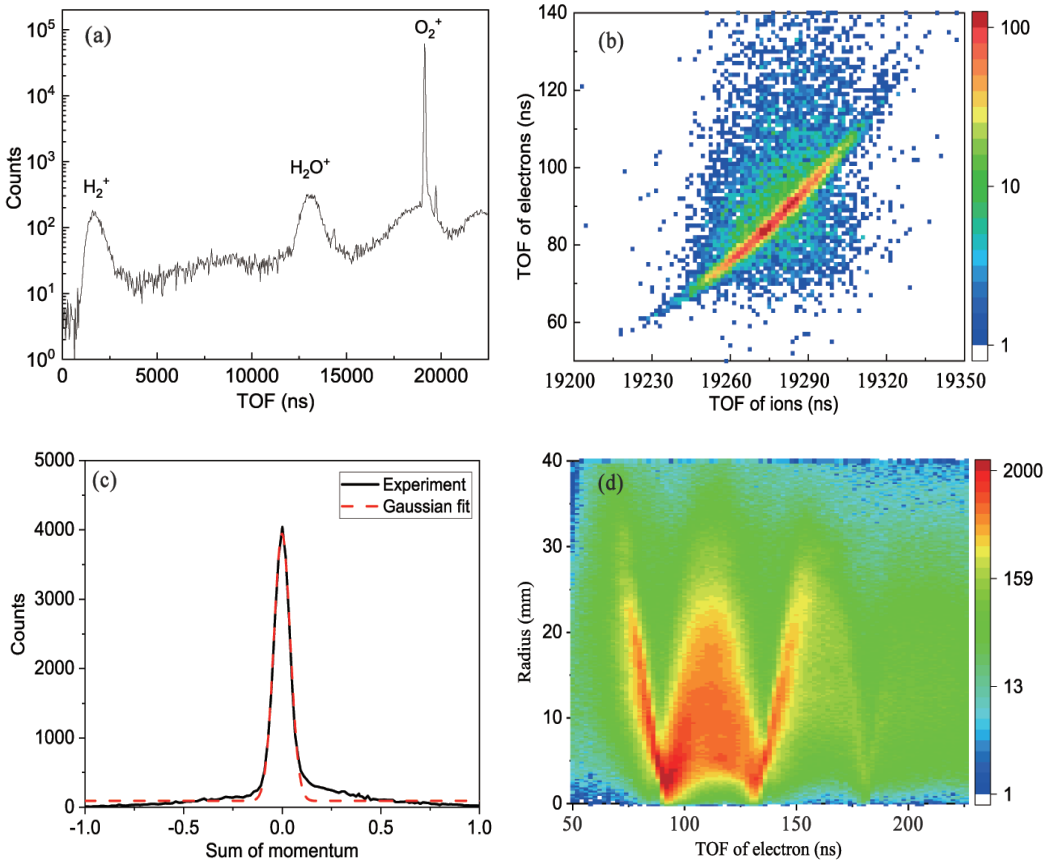

Figure 4. (**a**) TOF spectrum of a photo-ion for single ionization of oxygen; (**b**) TOF correlation spectrum of electron and O_2^+ ion ; (**c**) sum of momentum of electron and O_2^+ ion; (**d**) radius as a function of TOF for electrons.

3.2. Coulomb Explosion Experiment of Oxygen Moleculse

In the oxygen Coulomb explosion experiment, a femtosecond laser with 1.0×10^{15} W/cm^2-intensity and a polarization direction along the y axis interacted with the oxygen molecules. Due to the larger momentum from the Coulomb explosion, the accelerating electric field was set at 15 V/cm to ensure that all ions could be detected by the detector.

The ion fragments produced from both supersonic jet and the background gas were detected and the TOF spectra are shown in Figure 5, which shows that the composition of background gas was mainly water and hydrogen molecules. In contrast to the peaks of H_2O^+, H_2^+ and H^+ originating from the background, the O_2^+ peak is obviously sharper due to the different thermal properties between the warm residual gas and the cold jet. The O^{2+} peak is wider than O_2^+ peak, which indicates that a Coulomb explosion resulting in a larger kinetic energy occurred. At the TOF position, corresponding to a charge/mass ratio of 16 a.m.u./e, a narrow peak and a wide peak, which correspond to the O_2^{2+} ions from the ionization processes and the O^+ ions from the Coulomb explosion processes, respectively, are overlapped.

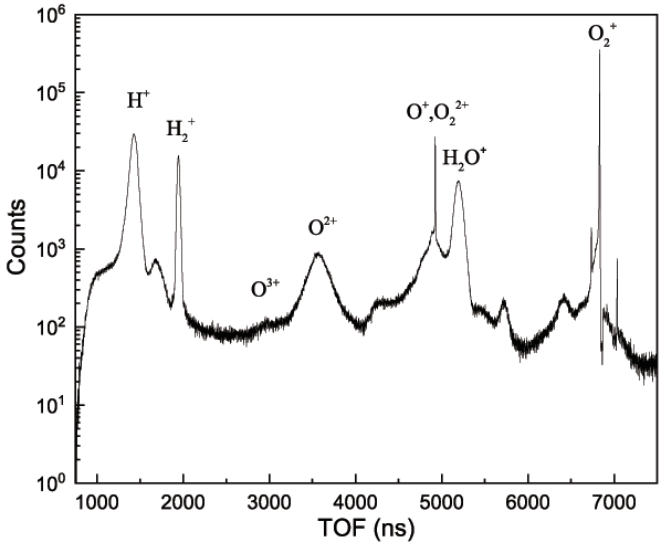

Figure 5. TOF spectrum of recoil ions.

Figure 6a presents the TOF correlation between the first ion and the second ion and five bright curves correspond to five different Coulomb explosion channels coming from two-to-five-fold charged oxygen ions. It can be seen from Figure 6b that most of the reaction products were within the range of the detector, and several distinctly separated rings appeared as a fingerprint of the Coulomb explosion, occurring in the polarization direction mostly. By calculating the momentum of all kinds of ions and sifting through the momentum conservation conditions, five Coulomb explosion channels were obtained including (1,1), (1,2), (1,3), (2,2) and (2,3).

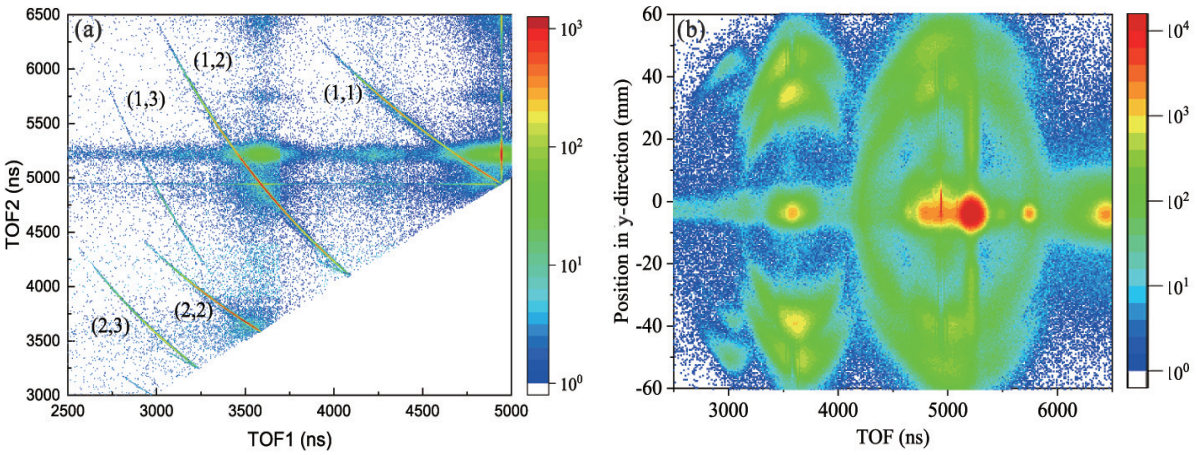

Figure 6. (**a**) Photoion–photoion coincidence (PIPICO) spectrum. The curve (m,n) represents the Coulomb explosion channels $O_2^{(m+n)+} \rightarrow O^{m+} + O^{n+}$. (**b**) TOF versus ion position in the y direction (the direction of the laser's polarization).

After the ion matching and data selection, more information on specific channel could be further analyzed. The released momenta were converted to their released kinetic energies. Figure 7 presents the peak distributions of kinetic energy releases for the four most distinct channels of (1,1), (1,2), (2,2) and (2,3), the peak positions of which were 11.3 eV, 20.5 eV, 35.1 eV and 49.6 eV, respectively. Compared with the previous results listed in Table 2, the measured KERs were generally smaller than those from electron and ion impact experiments, due to the stretched molecular bond length in the laser field, which is also consistent with other laser-induced fragmentation experiments [46,47]. On the other hand, Wu et al. found that the KERs become larger with increasing laser intensity [47].

The larger KER values indicated a higher laser intensity in our experiment. For example, the measured KER of 11.3 eV from the channel (1,1) was relatively larger compared with most KER peaks obtained in the 8-fs laser experiment [48] and smaller compared with the results from the electron impact experiment using Doppler-free spectroscopy [49].

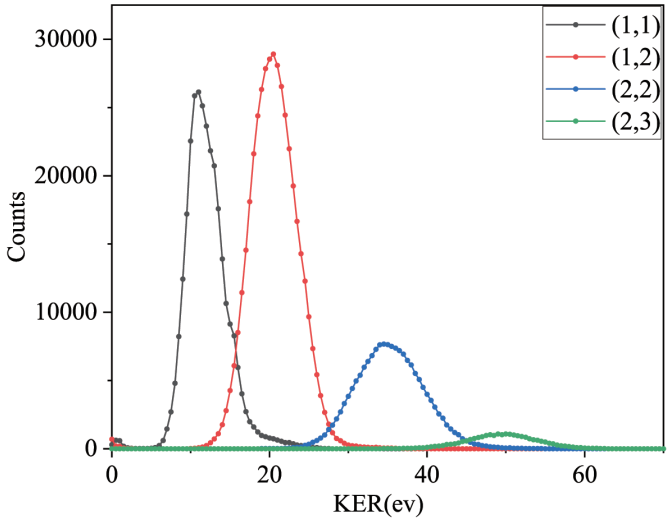

Figure 7. Kinetic energy releases of recoil ions in various channels.

Table 2. Kinetic energy release for the coulomb explosion of O_2^{x+} (x = 3–5) in the present experiment, together with previously reported results.

Channel	Present KER (eV)	Previous KER (eV)	Reference
(1,1)	11.3	7.4, 8.9, 9.6, 11.8	photon [48]
		11.2, 12.3, 12.7	electron [49]
(1,2)	20.5	13.5, 17.0	photon [50]
		15.9, 19.8, 31.2	ion [51]
(2,2)	35.1	24.8	photon [50]
		26, 30, 36	photon [52]
(2,3)	49.6	75	ion [53]

For the Coulomb explosion process of O_2^{2+}, extensive studies have been performed, both theoretically and experimentally [46,54]. Explosions of the parent dications are generally considered to occur near the equilibrium internuclear distance of the neutral molecule [50]. Assuming that the oxygen atomic ions are in the ground state ($O^+(^4S) + O^+(^4S)$), it can be inferred unambiguously by the KER and the potential energy curves of O_2^{2+} [49] that the electronic state of O_2^{2+} is B $^3\Pi_g$, which is an excited state. The electronic states of other parent ions cannot be identified directly, due to the non-vertical ionizing transition process, which leads to an energy defect. For multi-charged molecular ions O_2^{x+}, the repulsion of the charges drove the dissociation process, so the classic Coulomb explosion model was used to estimate the internuclear distances, R, where the explosion occurred [55]. They were calculated to be 1.40 Å, 1.64 Å and 1.74 Å from the corresponding KERs for channels (1,2), (2,2) and (2,3). This result showed that the O–O bonds, prior to the Coulomb explosion, were elongated and the internuclear distances before the explosion increased with increasing charge state, which is consistent with previous results [47,56].

4. Conclusions

In this work, a new multi-particle reaction microscope, constructed for studies of AMO science at the SXFEL, has been explored The supersonic gas jet, the design of its spectrometer and the data acquisition system containing the detectors have been described in detail. A cold gas target with a density of 10^8 atoms/cm^2 has been shown capable of

reacting with light at the center of the science chamber, where the vacuum is maintained at better than 1.2×10^{-10} torr. To test the performance of the device, a single ionization experiment and Coulomb explosion experiment of O_2 have been performed with a strong laser field at 10^{14} to 10^{15} W/cm^2 intensities. The momentum resolution is shown better than 0.11 a.u. for both ion and electron detection, and the experimental results from the Coulomb explosion processes are consistent with previous studies. It has been shown that the instrument can perform multi-particle coincidence measurements at a wide range of energies and detect the momenta of ions and electrons at full-solid angles. From the kinetic energy releases of the explosion channels, the electronic state of O_2^{2+} and the internuclear distances of multi-charged ions O_2^{x+} (x = 3–5) before the explosion have been deduced. The high resolution and good operation of the instrument provide us with a solid foundation for future atomic and molecular experiments at the Shanghai SXFEL facility.

5. Future Plan

In the near future, we plan to further improve the vacuum condition. Due to the strong light intensity of soft X-rays, a higher-vacuum environment is favorable for coincidence measurements. A pumping system with non-evaporate getter pumps is being prepared and is expected to increase the current vacuum by an order of magnitude. Additionally, we plan to design a new spectrometer that can switch between REMI mode and VMI mode in order to adapt to different experimental conditions. In addition, a fast analog-to-digital converter (fADC) system for data acquisition has been designed to improve the detection efficiency at a higher counting rate and retain the original data information completely, including the pulse heights and shapes of detector signals.

Author Contributions: Conceptualization, X.W. and Y.J.; validation, X.W., W.J., S.Z., Z.S., R.D., Y.G. and J.F.; formal analysis, W.J.; investigation, W.J.; data curation, W.J., X.W. and S.Z.; writing—original draft preparation, W.J.; writing—review and editing, S.Z., X.W. and Y.J.; project administration, Y.J. and Z.Z.; funding acquisition, Y.J. and Z.Z. All authors have read and agreed to the published version of the manuscript.

Funding: The work is supported by Shanghai-XFEL beamline project (SBP) (31011505505885920161A2101001) and National Natural Science Foundation of China (NSFC) (11827806).

Institutional Review Board Statement: Not applicable.

Informed Consent Statement: Not applicable.

Data Availability Statement: Not applicable.

Acknowledgments: We are grateful to Xueguang Ren, Wei Quan, Jiaming Jiang, Yuneng Shen, Tiqiao Xiao, Jianhui Chen and Zhi Liu for their valuable discussions and technical assistance.

Conflicts of Interest: The authors declare no conflict of interest. The founding sponsors had no role in the design of the study; in the collection, analyses or interpretation of data; in the writing of the manuscript; nor in the decision to publish the results.

References

1. Dörner, R.; Mergel, V.; Bräuning, H.; Achler, M.; Weber, T.; Khayyat, K.; Jagutzki, O.; Spielberger, L.; Ullrich, J.; Moshammer, R.; et al. Recoil ion momentum spectroscopy a 'momentum microscope' to view atomic collision dynamics. *AIP Conf. Proc.* **1998**, *443*, 334–346.
2. Dörner, R.; Mergel, V.; Jagutzki, O.; Spielberger, L.; Ullrich, J.H.; Moshammer, R.; Schmidt-Bocking, H. Cold target recoil ion momentum spectroscopy: A 'momentum microscope' to view atomic collision dynamics. *Phys. Rep.* **2000**, *330*, 95–192. [CrossRef]
3. Ullrich, J.; Moshammer, R.; Dorn, A.; Dörner, R.; Schmidt, L.P.H.; Schmidt-Böcking, H. Recoil-ion and electron momentum spectroscopy: Reaction-microscopes. *Rep. Prog. Phys.* **2003**, *66*, 1463–1545. [CrossRef]
4. Jahnke, T.; Mergel, V.; Jagutzki, O.; Czasch, A.; Ullmann, K.; Ali, R.; Frohne, V.; Weber, T.; Schmidt, L.; Eckart, S.; et al. High-Resolution Momentum Imaging—From Stern's Molecular Beam Method to the COLTRIMS Reaction Microscope. In *Molecular Beams in Physics and Chemistry: From Otto Stern's Pioneering Exploits to Present–Day Feats*; Springer: Cham, Switzerland, 2021; pp. 375–441. [CrossRef]
5. Ullrich, J.; Schmidt-Böcking, H. Time-of-flight spectrometer for the determination of microradian projectile scattering angles in atomic collisions. *Phys. Lett. A* **1987**, *125*, 193–196. [CrossRef]

6. Moshammer, R.; Ullrich, J.; Unverzagt, M.; Schmidt, W.; Jardin, P.; Olson, R.E.; Mann, R.; Dörner, R.; Mergel, V.; Buck, U.; et al. Low-Energy Electrons and Their Dynamical Correlation with Recoil Ions for Single Ionization of Helium by Fast, Heavy-Ion Impact. *Phys. Rev. Lett.* **1994**, *73*, 3371–3374. [CrossRef] [PubMed]
7. Moshammer, R.; Unverzagt, M.; Schmitt, W.; Ullrich, J.; Schmidt-Böcking, H. A 4π recoil-ion electron momentum analyzer: A high-resolution "microscope" for the investigation of the dynamics of atomic, molecular and nuclear reactions. *Nucl. Instrum. Methods Phys. Res. Sect. B Beam Interact. Mater. Atoms* **1996**, *108*, 425–445. [CrossRef]
8. Schmidt, H.; Cederquist, H.; Schuch, R.; Bagge, L.; Källberg, A.; Hilke, J.; Rensfelt, K.G.; Mergel, V.; Achler, M.; Dörner, R.; et al. A design study for an internal gas-jet target for the heavy-ion storage ring CRYRING. *Hyperfine Interact.* **1997**, *108*, 339–354.:1012635418262. [CrossRef]
9. Allspach, D.; Hahn, A.; Kendziora, C.; Pordes, S.; Boero, G.; Garzoglio, G.; Macri, M.; Marinelli, M.; Pallavicini, M.; Robutti, E. The variable density gas jet internal target for Experiment 835 at Fermilab. *Nucl. Instrum. Methods Phys. Res. Sect. A* **1998**, *410*, 195–205. [CrossRef]
10. Soukhanovskii, V.A.; Kugel, H.W.; Kaita, R.; Majeski, R.; Roquemore, A.L. Supersonic gas injector for fueling and diagnostic applications on the National Spherical Torus Experiment. *Rev. Sci. Instrum.* **2004**, *75*, 4320–4323. [CrossRef]
11. Amitay, Z.; Zajfman, D. A new type of multiparticle three-dimensional imaging detector with subnanosecond time resolution. *Rev. Sci. Instrum.* **1997**, *68*, 1387–1392. [CrossRef]
12. Oberheide, J.; Wilhelms, P.; Zimmer, M. RAPID COMMUNICATION: New results on the absolute ion detection efficiencies of a microchannel plate. *Meas. Sci. Technol.* **1997**, *8*, 351–354. [CrossRef]
13. Straub, H.; Mangan, M.; Lindsay, B.; Smith, K.; Stebbings, R. Absolute detection efficiency of a microchannel plate detector for kilo-electron volt energy ions. *Rev. Sci. Instrum.* **1999**, *70*, 4238–4240. [CrossRef]
14. Jagutzki, O.; Cerezo, A.; Czasch, A.; Dörner, R.; Hattas, M.; Huang, M.; Mergel, V.; Spillmann, U.; Ullmann-Pfleger, K.; Weber, T.; et al. Multiple hit readout of a microchannel plate detector with a three-layer delay-line anode. *IEEE Trans. Nucl. Sci.* **2002**, *49*, 2477–2483. [CrossRef]
15. Strickland, D.; Mourou, G. Compression of Amplified Chirped Optical Pulses. *Opt. Commun.* **1985**, *55*, 219–221. [CrossRef]
16. de Jesus, V.; Rudenko, A.; Feuerstein, B.; Zrost, K.; Schröter, C.; Moshammer, R.; Ullrich, J. Reaction microscopes applied to study atomic and molecular fragmentation in intense laser fields: Non-sequential double ionization of helium. *J. Electron Spectrosc. Relat. Phenom.* **2004**, *141*, 127–142. [CrossRef]
17. Sabbar, M.; Heuser, S.; Boge, R.; Lucchini, M.; Gallmann, L.; Cirelli, C.; Keller, U. Combining attosecond XUV pulses with coincidence spectroscopy. *Rev. Sci. Instrum.* **2014**, *85*, 103113. [CrossRef] [PubMed]
18. Schmid, G.; Schnorr, K.; Augustin, S.; Meister, S.; Lindenblatt, H.; Trost, F.; Liu, Y.; Braune, M.; Treusch, R.; Schröter, C.D.; et al. Reaction microscope endstation at FLASH2. *J. Synchrotron Radiat.* **2019**, *26*, 854–867. [CrossRef] [PubMed]
19. Ackermann, W.; Asova, G.; Ayvazyan, V.; Azima, A.; Baboi, N.; Bähr, J.; Balandin, V.; Beutner, B.; Brandt, A.; Bolzmann, A.; et al. Operation of a free-electron laser from the extreme ultraviolet to the water window. *Nat. Photonics* **2007**, *1*, 336–342. [CrossRef]
20. Seddon, E.A.; Clarke, J.A.; Dunning, D.J.; Masciovecchio, C.; Milne, C.J.; Parmigiani, F.; Rugg, D.; Spence, J.C.H.; Thompson, N.R.; Ueda, K.; et al. Short-wavelength free-electron laser sources and science: A review. *Rep. Prog. Phys.* **2017**, *80*, 115901. [CrossRef] [PubMed]
21. Berrah, N.; Bozek, J.; Costello, J.; Düsterer, S.; Fang, L.; Feldhaus, J.; Fukuzawa, H.; Hoener, M.; Jiang, Y.; Johnsson, P.; et al. Non-linear processes in the interaction of atoms and molecules with intense EUV and X-ray fields from SASE free electron lasers (FELs). *J. Mod. Opt.* **2010**, *57*, 1015–1040. [CrossRef]
22. Ullrich, J.; Rudenko, A.; Moshammer, R. Free-Electron Lasers: New Avenues in Molecular Physics and Photochemistry. *Annu. Rev. Phys. Chem.* **2012**, *63*, 635–660. [CrossRef]
23. Zhang, Y.Z.; Jiang, Y.H. Imaging Ultra-fast Molecular Dynamics in Free Electron Laser Field. In *Advances of Atoms and Molecules in Strong Laser Fields*; World Scientific: Singapore, 2015; Chapter 8, pp. 205–235._0008. [CrossRef]
24. Young, L.; Ueda, K.; Gühr, M.; Bucksbaum, P.H.; Simon, M.; Mukamel, S.; Rohringer, N.; Prince, K.C.; Masciovecchio, C.; Meyer, M.; et al. Roadmap of ultrafast X-ray atomic and molecular physics. *J. Phys. B At. Mol. Opt. Phys.* **2018**, *51*, 032003. [CrossRef]
25. Callegari, C.; Grum-Grzhimailo, A.N.; Ishikawa, K.L.; Prince, K.C.; Sansone, G.; Ueda, K. Atomic, molecular and optical physics applications of longitudinally coherent and narrow bandwidth Free-Electron Lasers. *Phys. Rep.* **2021**, *904*, 1–59. [CrossRef]
26. Moshammer, R.; Jiang, Y.H.; Foucar, L.; Rudenko, A.; Ergler, T.; Schröter, C.D.; Lüdemann, S.; Zrost, K.; Fischer, D.; Titze, J.; et al. Few-Photon Multiple Ionization of Ne and Ar by Strong Free-Electron-Laser Pulses. *Phys. Rev. Lett.* **2007**, *98*, 203001. [CrossRef]
27. Jiang, Y.H.; Rudenko, A.; Kurka, M.; Kühnel, K.U.; Ergler, T.; Foucar, L.; Schöffler, M.; Schössler, S.; Havermeier, T.; Smolarski, M.; et al. Few-Photon Multiple Ionization of $\mathbf{N}_2$ by Extreme Ultraviolet Free-Electron Laser Radiation. *Phys. Rev. Lett.* **2009**, *102*, 123002. [CrossRef] [PubMed]
28. Jiang, Y.H.; Rudenko, A.; Perez-Torres, J.; Herrwerth, O.; Foucar, L.; Kurka, M.; Kühnel, K.; Toppin, M.; Plésiat, E.; Morales, F.; et al. Investigating two-photon double ionization of D2 by XUV-pump-XUV-probe experiments. *Phys. Rev. A* **2010**, *81*, 051402. [CrossRef]
29. Jiang, Y.H.; Rudenko, A.; Plésiat, E.; Foucar, L.; Kurka, M.; Kühnel, K.U.; Ergler, T.; Pérez-Torres, J.F.; Martín, F.; Herrwerth, O.; et al. Tracing direct and sequential two-photon double ionization of D_2 in femtosecond extreme-ultraviolet laser pulses. *Phys. Rev. A* **2010**, *81*, 021401. [CrossRef]

30. Magrakvelidze, M.; Herrwerth, O.; Jiang, Y.H.; Rudenko, A.; Kurka, M.; Foucar, L.; Kühnel, K.U.; Kübel, M.; Johnson, N.G.; Schröter, C.D.; et al. Tracing nuclear-wave-packet dynamics in singly and doubly charged states of N_2 and O_2 with XUV-pump–XUV-probe experiments. *Phys. Rev. A* **2012**, *86*, 013415. [CrossRef]
31. Jiang, Y.H.; Rudenko, A.; Herrwerth, O.; Foucar, L.; Kurka, M.; Kühnel, K.U.; Lezius, M.; Kling, M.F.; van Tilborg, J.; Belkacem, A.; et al. Ultrafast Extreme Ultraviolet Induced Isomerization of Acetylene Cations. *Phys. Rev. Lett.* **2010**, *105*, 263002. [CrossRef]
32. Li, Z.; Inhester, L.; Liekhus-Schmaltz, C.; Curchod, B.; Snyder, J.; Medvedev, N.; Cryan, J.; Osipov, T.; Pabst, S.; Vendrell, O.; et al. Ultrafast isomerization in acetylene dication after carbon K-shell ionization. *Nat. Commun.* **2017**, *8*, 453. [CrossRef]
33. Young, L.; Kanter, E.; Krässig, B.; Li, Y.; March, A.; Pratt, T.; Santra, R.; Southworth, S.; Rohringer, N.; Dimauro, L.; et al. Femtosecond electronic response of atoms to ultra-intense X-rays. *Nature* **2010**, *466*, 56–61. [CrossRef] [PubMed]
34. Rudenko, A.; Inhester, L.; Hanasaki, K.; Li, X.; Robatjazi, S.J.; Erk, B.; Boll, R.; Toyota, K.; Hao, Y.; Vendrell, O.; et al. Femtosecond response of polyatomic molecules to ultra-intense hard X-rays. *Nature* **2017**, *546*, 129–132. [CrossRef] [PubMed]
35. Nagler, B.; Zastrau, U.; Fäustlin, R.; Vinko, S.; Whitcher, T.; Nelson, A.; Sobierajski, R.; Krzywinski, J.; Chalupský, J.; Abreu, E.; et al. Turning solid aluminium transparent by intense soft X-ray photoionization. *Nat. Phys.* **2009**, *5*, 693–696. [CrossRef]
36. Carpeggiani, P.; Gryzlova, E.; Reduzzi, M.; Dubrouil, A.; Faccialà, D.; Negro, M.; Ueda, K.; Burkov, S.; Frassetto, F.; Stienkemeier, F.; et al. Complete reconstruction of bound and unbound electronic wavefunctions in two-photon double ionization. *Nat. Phys.* **2019**, *15*, 170–177. [CrossRef]
37. Loriot, V.; Marciniak, A.; Karras, G.; Schindler, B.; Renois-Predelus, G.; Compagnon, I.; Concina, B.; Brédy, R.; Celep, G.; Bordas, C.; et al. Angularly resolved RABBITT using a second harmonic pulse. *J. Opt.* **2017**, *19*, 114003. [CrossRef]
38. Meyer, M.; Grum-Grzhimailo, A.N.; Cubaynes, D.; Felfli, Z.; Heinecke, E.; Manson, S.T.; Zimmermann, P. Magnetic Dichroism in *K*-Shell Photoemission from Laser Excited Li Atoms. *Phys. Rev. Lett.* **2011**, *107*, 213001. [CrossRef] [PubMed]
39. Demekhin, P.V.; Artemyev, A.N.; Kastner, A.; Baumert, T. Photoelectron Circular Dichroism with Two Overlapping Laser Pulses of Carrier Frequencies ω and 2ω Linearly Polarized in Two Mutually Orthogonal Directions. *Phys. Rev. Lett.* **2018**, *121*, 253201. [CrossRef] [PubMed]
40. Ngoko Djiokap, J.M.; Meremianin, A.; Manakov, N.; Madsen, L.; Hu, S.; Starace, A. Molecular Symmetry-Mixed Dichroism in Double Photoionization of H_2. *Phys. Rev. Lett.* **2019**, *123*, 143202. [CrossRef]
41. Kastirke, G.; Schöffler, M.S.; Weller, M.; Rist, J.; Boll, R.; Anders, N.; Baumann, T.M.; Eckart, S.; Erk, B.; De Fanis, A.; et al. Photoelectron Diffraction Imaging of a Molecular Breakup Using an X-ray Free-Electron Laser. *Phys. Rev. X* **2020**, *10*, 021052. [CrossRef]
42. Zhao, Z.; Wang, D.; Gu, Q.; Yin, L.; Gu, M.; Leng, Y.; Liu, B. Status of the SXFEL Facility. *Appl. Sci.* **2017**, *7*, 607. [CrossRef]
43. Miller, D. Free Jet Sources. *At. Mol. Beam Methods* **1988**, *1*, 14–53.
44. Hillenkamp, M.; Keinan, S.; Even, U. Condensation limited cooling in supersonic expansions. *J. Chem. Phys.* **2003**, *118*, 8699–8705. [CrossRef]
45. Lampton, M.; Siegmund, O.; Raffanti, R. Delay line anodes for microchannel-plate spectrometers. *Rev. Sci. Instrum.* **1987**, *58*, 2298–2305. [CrossRef]
46. Chelkowski, S.; Bandrauk, A.D. Two-step Coulomb explosions of diatoms in intense laser fields. *J. Phys. B At. Mol. Opt. Phys.* **1995**, *28*, L723–L731. [CrossRef]
47. Wu, J.; Zeng, H.; Guo, C. Vertical and nonvertical transitions in triple-ionization-induced dissociation of diatomic molecules. *Phys. Rev. A* **2006**, *74*, 065403. [CrossRef]
48. Alnaser, A.S.; Voss, S.; Tong, X.M.; Maharjan, C.M.; Ranitovic, P.; Ulrich, B.; Osipov, T.; Shan, B.; Chang, Z.; Cocke, C.L. Effects Of Molecular Structure on Ion Disintegration Patterns In Ionization of O_2 and N_2 by Short Laser Pulses. *Phys. Rev. Lett.* **2004**, *93*, 113003. [CrossRef]
49. Lundqvist, M.; Edvardsson, D.; Baltzer, P.; Larsson, M.; Wannberg, B. Observation of predissociation and tunnelling processes in O_2^{2+}: A study using Doppler free kinetic energy release spectroscopy and ab initio CI calculations. *J. Phys. B At. Mol. Opt. Phys.* **1996**, *29*, 499. [CrossRef]
50. Wu, C.; Yang, Y.; Wu, Z.; Chen, B.; Dong, H.; Liu, X.; Deng, Y.; Liu, H.; Liu, Y.; Gong, Q. Coulomb explosion of nitrogen and oxygen molecules through non-Coulombic states. *Phys. Chem. Chem. Phys.* **2011**, *13*, 18398–18408. [CrossRef]
51. Horvat, V.; Watson, R. 3D momentum imaging of molecular dissociation induced by fast, heavy-ion collisions in the strong interaction regime. *Nucl. Instrum. Methods Phys. Res. Sect. B Beam Interact. Mater. Atoms* **2011**, *269*, 2584–2592. [CrossRef]
52. Cornaggia, C.; Quaglia, L. Experimental observation of non-Coulombic states of transient multicharged molecular ions N_2^{4+} and O_2^{4+}. *Phys. Rev. A* **2001**, *63*, 030702. [CrossRef]
53. Werner, U.; SiegTmann, B.; Mann, R.; Kabachnik, N.M.; Lutz, H.O. Kinetic Energy Release Distributions in the Fragmentation of O_2 Molecules Induced by Fast Highly Charged Ions. *Phys. Scr.* **2001**, *T92*, 244–247. [CrossRef]
54. Normand, D.; Cornaggia, C.; Lavancier, J.; Morellec, J.; Liu, H. Multielectron dissociative ionization of O_2 in an intense picosecond laser field. *Phys. Rev. A* **1991**, *44*, 475–482. [CrossRef] [PubMed]
55. Codling, K.; Frasinski, L.J.; Hatherly, P.A. On the field ionisation of diatomic molecules by intense laser fields. *J. Phys. B At. Mol. Opt. Phys.* **1989**, *22*, L321–L327. [CrossRef]
56. Wu, Z.; Wu, C.; Liu, X.; Liu, Y.; Deng, Y.; Gong, Q. Multiple ionization of oxygen studied by coincident measurement. *Opt. Express* **2010**, *18*, 10395–10403. [CrossRef]